Spherical Wavefronts Improve MU-MIMO Spectral Efficiency When Using Electrically Large Arrays

Giacomo Bacci, *Member, IEEE*, Luca Sanguinetti, *Senior Member, IEEE*, and Emil Björnson, *Fellow, IEEE*

***Abstract*—Modern multiple-input multiple-output (MIMO) communication systems are almost exclusively designed assuming locally plane wavefronts over antenna arrays. This is known as the *far-field approximation* and is soundly justified at sub-6-GHz frequencies at most relevant transmission ranges. However, when higher frequencies and shorter transmission ranges are used, the wave curvature over the array is no longer negligible, and arrays operate in the so-called *radiative near-field region*. This letter aims to show that the classical far-field approximation may significantly underestimate the achievable spectral efficiency of multi-user MIMO communications operating in the 30-GHz bands and above, even at ranges beyond the Fraunhofer distance. For planar arrays with typical sizes, we show that computing combining schemes based on the far-field model significantly reduces channel gain and spatial multiplexing capability. When the radiative near-field model is used, interference rejection schemes, such as the optimal minimum mean-square-error combiner, appear to be very promising, when combined with electrically large arrays, to meet the requirements of next-generation networks.**

***Index Terms*—Near-field focusing, mm-Wave and sub-THz communications, Fraunhofer distance, spherical wavefronts.**

I. Introduction and Motivation

THE INCREASING demand for ubiquitous, reliable, fast, and scalable wireless services is pushing today's radio technology toward its ultimate limits. In this context, it is natural to continue searching for more bandwidth, which in turn pushes the operation towards higher frequencies [1]. 5G is designed to operate in bands up to 71 GHz [2]. Terahertz (THz) communications in the band from 0.1 to 10 THz is considered as a highly promising technology for 6G and beyond [1]. The use of high frequencies translates into higher path losses per antenna, which can be compensated for by antenna arrays. This combination undermines a fundamental assumption of multiple antenna communications: *the wavefronts of radiated waves are locally planar over antenna arrays* [3].

Manuscript received 17 February 2023; revised 6 April 2023; accepted 13 April 2023. Date of publication 18 April 2023; date of current version 11 July 2023. This work was supported in part by the University of Pisa under Grant PRA 2022 91 INTERCONNECT. The work of Giacomo Bacci and Luca Sanguinetti was supported in part by the Italian Ministry of Education and Research (MUR) in the Framework of the FoReLab Project (Departments of Excellence). The work of Emil Björnson was supported by SSF under Grant FFL18-0277. The associate editor coordinating the review of this article and approving it for publication was Q. Wu. *(Corresponding author: Giacomo Bacci.)*

Giacomo Bacci and Luca Sanguinetti are with the Dip. Ingegneria dell'Informazione, University of Pisa, 56122 Pisa, Italy (e-mail:giacomo.bacci;luca.sanguinetti@unipi.it).

Emil Björnson is with the Department of Computer Science, KTH Royal Institute of Technology, 10044 Stockholm, Sweden (e-mail: emilbjo@kth.se).

Digital Object Identifier 10.1109/LWC.2023.3268087

When an antenna radiates a wireless signal in free space, the wavefront of electromagnetic waves has a different shape depending on the distance. Traditionally, two regions have been distinguished [4]: the Fresnel and the far-field (FF) regions. Wireless communications have almost exclusively operated in the FF, which conventionally assumes propagation distances beyond the Fraunhofer one. When arrays between 10 cm and 1 m are utilized, typical ranges up to 100 m are almost entirely in the Fresnel region when using a carrier frequency in the range 30–300 GHz [5]. Thus, plane wave approximation does not hold anymore, and spherical wavefront propagation must be considered instead [5]. This enables spatial-multiplexing in low-rank single-user MIMO systems [6], [7] and for high-accuracy estimation of source position [8]. However, this line of research constitutes a minor fraction of the vast literature based on plane-wave approximation.

Our objective is to show that, in the bands above 6 GHz, the classical FF approximation may profoundly underestimate the achievable performance of multi-user MIMO communication systems equipped with planar arrays of practical size, i.e., in the order of half-a-meter. The underestimation is already large in the mm-Wave band around 30 GHz bands, and is further exacerbated when higher frequencies are considered. Our numerical analysis also shows that, when the radiative near-field (NF) channel model is used, minimum mean-square-error (MMSE) combining vastly outperforms maximum ratio (MR), thanks to the sub-wavelength spatial resolution that largely increases its interference suppression capabilities. Particularly, MMSE combining enables serving very many user equipments (UEs) in the order of 1500 UEs/km^2 per channel use (in line with 5G requirements [9]), while ensuring fairness across them (and thus significantly increasing the performance at the cell edge). This makes the combination of MMSE combining and electrically large arrays a promising candidate to meet the stringent capacity requirements of next-generation networks.

II. System and Signal Model

We consider the planar array shown in Fig. 1. The array consists of N_{V} horizontal rows and N_{H} antennas per row, for a total of $N = N_{\mathsf{H}} N_{\mathsf{V}}$ antennas. Each antenna has an area A and the spacing is d_{H} and d_{V} along the horizontal and vertical directions, respectively. Thus, the horizontal and vertical lengths of the array are $L_{\mathsf{H}} = N_{\mathsf{H}}\sqrt{A} + (N_{\mathsf{H}} - 1)d_{\mathsf{H}}$ and $L_{\mathsf{V}} = N_{\mathsf{V}}\sqrt{A} + (N_{\mathsf{V}} - 1)d_{\mathsf{V}}$, respectively. The antennas are numbered from left to right and from the bottom row to the top row so that antenna n is located at $\mathbf{r}_n = [x_n, y_n, 0]^{\mathsf{T}}$, where $x_n = \Delta_{\mathsf{H}}(-\frac{N_{\mathsf{H}}-1}{2} + \mathrm{mod}(n-1, N_{\mathsf{H}}))$ and $y_n = \Delta_{\mathsf{V}}(-\frac{N_{\mathsf{V}}-1}{2} + \lfloor (n-1)/N_{\mathsf{H}} \rfloor)$ with $\Delta_{\mathsf{H}} = \sqrt{A} + d_{\mathsf{H}}$ and $\Delta_{\mathsf{V}} = \sqrt{A} + d_{\mathsf{V}}$. We assume that K single-antenna UEs are

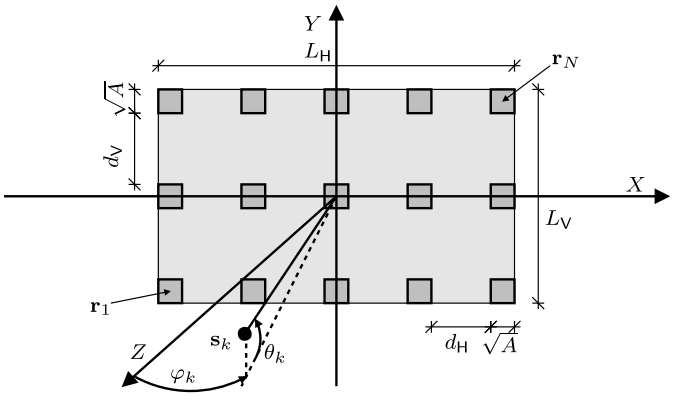

Fig. 1. Diagram of the 2D planar array located in the *XY*-plane.

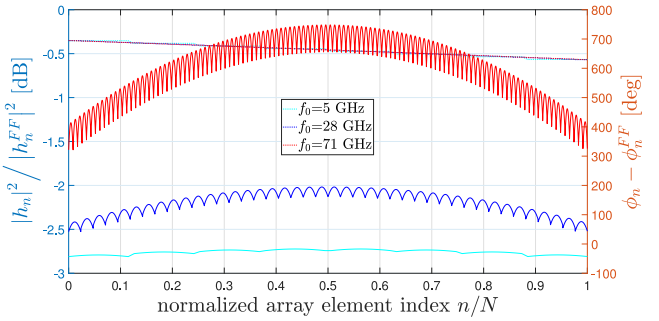

Fig. 2. Difference in the amplitude (left axis) and phase (right axis) between the exact model and the FF approximation.

active and transmit *Y*-polarized signals when traveling in the *Z* direction [10].[1] Line-of-sight (LoS) propagation is considered, as it becomes predominant at high frequencies [5]. We denote by $\mathbf{s}_k = [x_k, y_k, z_k]^{\mathsf{T}}$ the arbitrary location for source k and call $\varphi_k = \tan^{-1}(x_k/z_k)$ and $\theta_k = \tan^{-1}(y_k/\sqrt{x_k^2 + z_k^2})$ its azimuth and elevation angles, respectively.

We let $\mathbf{h}_k = [h_{k1}, \ldots, h_{kN}]^{\mathsf{T}} \in \mathbb{C}^N$ denote the channel of UE k. In particular, $h_{kn} = |h_{kn}|e^{-\mathrm{j}\phi_{kn}}$ is the channel from source k to receive antenna n, with $|h_{kn}|^2$ being the channel gain and $\phi_{kn} \in [0, 2\pi)$ the phase shift. In the remainder, perfect channel state information is assumed, since the channels $\{\mathbf{h}_k\}_{k=1}^K$ can be estimated arbitrarily well from pilot signals, thanks to the LoS propagation.

A. Channel Model

To model $\mathbf{h}_k$, we extend the prior work [10], which only considers the case $d_{\mathsf{H}} = d_{\mathsf{V}} = \sqrt{A}$. The extension to the case $d_{\mathsf{H}} \neq d_{\mathsf{V}}$ with $d_{\mathsf{H}}, d_{\mathsf{V}} \geq \sqrt{A}$ is as follows.

Corollary 1: Consider a lossless isotropic antenna located at $\mathbf{s}_k$ that transmits a *Y*-polarized signal when traveling in the *Z* direction. The free-space channel gain ζ_{kn} at receive antenna n, located at $\mathbf{r}_n$ is given by (1), shown at the bottom of the page, where

$$g_i(\alpha) \triangleq \sqrt{A}/2 + (-1)^i \alpha \tag{2}$$

while $x_{kn} = x_k - x_n$ and $y_{kn} = y_k - y_n$.

From Corollary 1, the following model is obtained.

Corollary 2 (Exact Model): The channel entry $h_{kn} = |h_{kn}|e^{-\mathrm{j}\phi_{kn}}$ is obtained as

$$|h_{kn}| = \sqrt{\zeta_{k,n}}, \qquad \phi_{kn} = 2\pi \bmod \left(\frac{\|\mathbf{d}_{kn}\|}{\lambda}, 1\right) \tag{3}$$

where ζ_{kn} is defined in (1) and $\mathbf{d}_{kn} = \mathbf{s}_k - \mathbf{r}_n$.

The above model provides a general expression for h_{kn} that allows to quantify its channel gain in the so-called *radiative NF* of the array [10], [11].[2] Since it captures the fundamental properties of wave propagation, we call it the *exact model*. Notice that it is substantially different from the classical *FF model*, e.g., [3], that assumes locally planar wavefronts over arrays and is valid for distances beyond the Fraunhofer distance $d_F = 2(L_{\mathsf{H}}^2 + L_{\mathsf{V}}^2)/\lambda$ [12, eq. (3)].

Corollary 3 (FF Approximation): If UE k is in the FF region of the array, i.e., $d_k \cos\varphi_k \gg \max(L_{\mathsf{H}}, L_{\mathsf{V}})$, then $h_{kn} \approx h_{kn}^{\mathrm{FF}}$ with $h_{kn}^{\mathrm{FF}} = |h_{kn}^{\mathrm{FF}}|e^{-\mathrm{j}\phi_{kn}}$ being modeled as

$$\left|h_{kn}^{\mathrm{FF}}\right| = \sqrt{\frac{A\cos\varphi_k}{4\pi d_k^2}}, \qquad \phi_{kn}^{\mathrm{FF}} = \mathbf{k}^{\mathsf{T}}(\varphi_k, \theta_k)\mathbf{r}_n \tag{4}$$

where $\mathbf{k}(\varphi_k, \theta_k) = \frac{2\pi}{\lambda}[\cos\theta_k \sin\varphi_k, \sin\theta_k, \cos\theta_k \cos\varphi_k]^{\mathsf{T}}$ is the wave vector, e.g., [13].

We notice that the propagation channel in MIMO systems has been almost exclusively modeled as in Corollary 3. For modern arrays of cellular networks[3] of size $1 \times 0.5\,\mathrm{m}^2$, this is a justified assumption when sub-6 GHz bands are used. In this case, $d_F \leq 50\,\mathrm{m}$ and, thus, most receivers are in the FF of the transmitter. The situation changes substantially in the frequency range 30-300 GHz, in which $d_F \geq 250\,\mathrm{m}$, and typical operating distances are entirely below it. This implies that the FF approximation cannot be used, and the exact propagation model derived in Corollary 1 must be considered instead. As is known, the radiative NF can create both noticeable amplitude variations and phase variations over the wavefront. To measure the impact of such variations, Fig. 2 reports the results for $L_{\mathsf{H}} = 0.5\,\mathrm{m}$, $L_{\mathsf{V}} = 1.0\,\mathrm{m}$, $A = (\lambda/4)^2$, $d_{\mathsf{H}} = 0.5\lambda$, and $d_{\mathsf{H}} = 2\lambda$, considering a UE located at 30 m from the base station (BS), which is elevated by 10 m. Amplitude variations are reported with dotted lines (using the left axis), whereas phase variations are represented by the solid lines (using the right axis). While the amplitude variations are negligible, the phase variations are significant, particularly when the carrier frequency increases. Please note that this may not hold true if

[1]The analysis can be extended to other polarization dimensions (e.g., linear combination of *X* and *Y* polarizations).

[2]Throughout this letter, we assume $\|\mathbf{d}_{kn}\| \gg \lambda$, so that the system, although in the NF region of the array, does not operate in the reactive NF of the transmit antenna (see [10], [11] for details).

[3]For instance, the Ericsson AIR 6419 product that contains 64 antenna-integrated radios in a box that is roughly $1 \times 0.5\,\mathrm{m}^2$ [14].

$$\zeta_{kn} = \frac{1}{12\pi}\sum_{i=0}^{1}\sum_{j=0}^{1}\frac{g_i(x_{kn})g_j(y_{kn})|z_k|}{\left(g_j^2(y_{kn}) + z_k^2\right)\sqrt{g_i^2(x_{kn}) + g_j^2(y_{kn}) + z_k^2}} + \frac{1}{6\pi}\sum_{i=0}^{1}\sum_{j=0}^{1}\tan^{-1}\left(\frac{g_i(x_{kn})g_j(y_{kn})}{|z_k|\sqrt{g_i^2(x_{kn}) + g_j^2(y_{kn}) + z_k^2}}\right) \tag{1}$$

the array size grows. Particularly, amplitude variations should be taken into account if one is interested in the asymptotic analysis of the system.

Note that the model in Corollary 1 is also accurate in the FF, thus there is no need to determine beforehand if the communication scenario is in the radiative NF region or not. Note that the above discussion does not require the use of *physically large arrays* (cf. [15], in which the array size is in the order of some squared meters), but holds true for currently available commercially-sized arrays, e.g., in the order of half-a-meter wide and height. What matters is the size relative to the wavelength, the so-called *electromagnetic size*.

B. System Model

We consider the uplink, in which the received signal is modeled as $\mathbf{y} \in \mathbb{C}^N = \sum_{k=1}^K \mathbf{h}_k s_k + \mathbf{n}$, where $s_k \sim \mathcal{N}_{\mathbb{C}}(0, p_k)$ is the data from UE k and $\mathbf{n} \in \mathbb{C}^N$ is the thermal noise with i.i.d. elements distributed as $\mathcal{N}_{\mathbb{C}}(0, \sigma^2)$. To decode s_k, $\mathbf{y}$ is processed with the combining vector $\mathbf{v}_k \in \mathbb{C}^N$. By treating the interference as noise, the spectral efficiency (SE) for UE k is $\log_2(1+\gamma_k)$, where

$$\gamma_k = \frac{p_k \left| \mathbf{v}_k^{\mathsf{H}} \mathbf{h}_k \right|^2}{\sum_{i \neq k} p_i \left| \mathbf{v}_k^{\mathsf{H}} \mathbf{h}_i \right|^2 + \sigma^2 \|\mathbf{v}_k\|^2} \tag{5}$$

is the signal-to-interference-plus-noise ratio (SINR). We consider both MR and MMSE combining. MR has low computational complexity and maximizes the power of the desired signal, but neglects interference. MMSE has higher complexity but it maximizes the SINR in (5). Other suboptimal schemes, e.g., zero-forcing, are not considered for space limitation. In the first case, $\mathbf{v}_k^{\mathrm{MR}} = \mathbf{h}_k / \|\mathbf{h}_k\|$, while in the second case

$$\mathbf{v}_k^{\mathrm{MMSE}} = \left(\sum_{i=1}^K p_i \mathbf{h}_i \mathbf{h}_i^{\mathsf{H}} + \sigma^2 \mathbf{I}_N \right)^{-1} \mathbf{h}_k \tag{6}$$

with $\mathbf{I}_N$ being the identity matrix of order N.

The vast majority of MIMO literature for high frequencies (e.g., in the mm-Wave bands) rely on the FF approximation in Corollary 3 and, instead of estimating $\mathbf{h}_k$ directly, estimate the three parameters $\{d_k, \theta_k, \varphi_k\}$. The latter are used to estimate $\{\mathbf{h}_k^{\mathrm{FF}}; k = 1, \ldots, K\}$ through (4), which are eventually used to compute the combiner. If the communication scenario is in the radiative NF region, then the system operates inevitably in a *mismatched mode*, no matter how good $\{d_k, \theta_k, \varphi_k\}$ have been estimated. From the above discussion, it thus follows that the combining vectors $\{\mathbf{v}_k\}_{k=1}^K$ can in practice follow either the *exact model* defined in Corollary 2 or the FF approximation defined in Corollary 3. The aim of this letter is to quantify the impact of such inaccurate channel modeling.

III. The Impact of a Mismatched Design

We assume that the BS is located at a height of $b = 10\,\mathrm{m}$. We further assume the following parameters, in line with the form factor of current 5G arrays: $L_{\mathsf{H}} = 0.5\,\mathrm{m}$, $L_{\mathsf{V}} = 1.0\,\mathrm{m}$, $A = (\lambda/4)^2$, $d_{\mathsf{H}} = 0.5\lambda$ and $d_{\mathsf{V}} = 2\lambda$. The communication takes places over a bandwidth of $B = 100\,\mathrm{MHz}$, with the total receiver noise power $\sigma^2 = -87\,\mathrm{dBm}$. Each UE transmits with power $p_k = 20\,\mathrm{dBm}\ \forall k$. We assume a carrier frequency of $f_0 = 28\,\mathrm{GHz}$ such that $\lambda = 10.71\,\mathrm{mm}$, $N_{\mathsf{H}} = 62$, and $N_{\mathsf{V}} = 42$, to focus on a 5G hot-spot scenario. When relevant, throughout this letter, we also consider higher carrier frequencies that cover future use cases and scenarios.

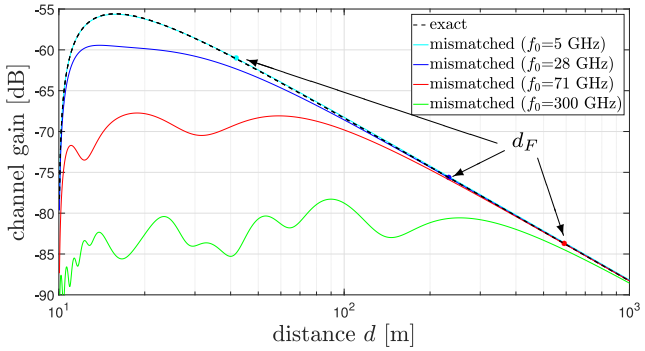

Fig. 3. Normalized channel gain $|\mathbf{v}_1^{\mathsf{H}}\mathbf{h}_1|^2/\|\mathbf{v}_1\|^2$ as a function of the distance of UE 1 along Z axis.

A. Channel Gain

We assume UE 1 to be located along the Z axis with coordinates $\mathbf{s}_1 = [0, -b, d]^{\mathsf{T}}$. In Fig. 3, the dashed black line reports the normalized channel gain $|\mathbf{v}_1^{\mathsf{H}}\mathbf{h}_1|^2/\|\mathbf{v}_1\|^2$ achieved with the exact model, whereas solid lines correspond to the channel gain measured with the combiners based on the FF model. Particularly, cyan and blue lines refers to the cases $f_0 = 5\,\mathrm{GHz}$ and $f_0 = 28\,\mathrm{GHz}$, respectively, whereas the red and the green lines refer to $f_0 = 71\,\mathrm{GHz}$ and $f_0 = 300\,\mathrm{GHz}$, respectively. Markers correspond to the Fraunhofer distances, obtained as $d_F = 2(L_{\mathsf{H}}^2 + L_{\mathsf{V}}^2)/\lambda$ [12, eq. (3)]. For $f_0 = 300\,\mathrm{GHz}$, $d_F = 2.5\,\mathrm{km}$ falls outside the selected range.

We see that, thanks to the large values of N, the channel gain with the exact model depends very weakly on the carrier frequency (a difference of at most 0.3 dB between 5 and 300 GHz at the local maximum of the curve), and we thus only report one line, for clarity. The same channel gain is achieved with the mismatched model only for sub-6 GHz frequencies, irrespective of the distance. This validates the accuracy of the FF approximation for such frequency bands. On the contrary, if higher frequencies are considered, then large differences are observed for transmission ranges below the Fraunhofer distance. This is a direct consequence of the inaccuracy of the FF approximation in the Fresnel region. The gap increases as f_0 increases. Interestingly, we observe that, for transmission ranges of practical interest (up to a hundred of meters), it is significant already for $f_0 \geq 71\,\mathrm{GHz}$. Finally, note that the normalized channel gain is not monotonically decreasing as the distance from the BS increases, but shows a local maximum. This is due to the specific choice of the BS height b: when the UE is too close to the BS, the smaller path loss is overwhelmed by the loss due to the array directivity at larger elevations. Thus, the local maximum increases as b increases.

B. Interference Gain

We now analyze the normalized interference gain $|\mathbf{v}_1^{\mathsf{H}}\mathbf{h}_2|^2/\|\mathbf{v}_1\|^2$ with the exact and mismatched models. We assume UE 1 is placed at a fixed position along the Z axis $\mathbf{s}_1 = [0, -10\,\mathrm{m}, +20\,\mathrm{m}]^{\mathsf{T}}$, whereas the interfering UE 2 is transmitting from different locations $\mathbf{s}_2 = [x_2, -10\,\mathrm{m}, z_2]^{\mathsf{T}}$

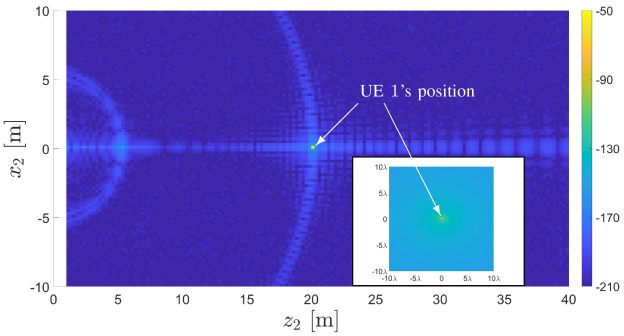

(a) MMSE combining.

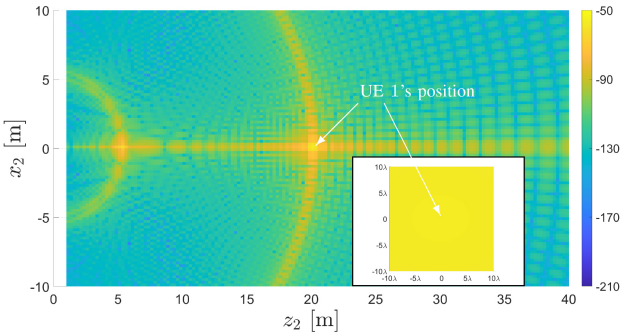

(b) MR combining.

Fig. 4. Interference gain behavior using the *exact* model for a fixed UE as a function of different locations of an interfering UE.

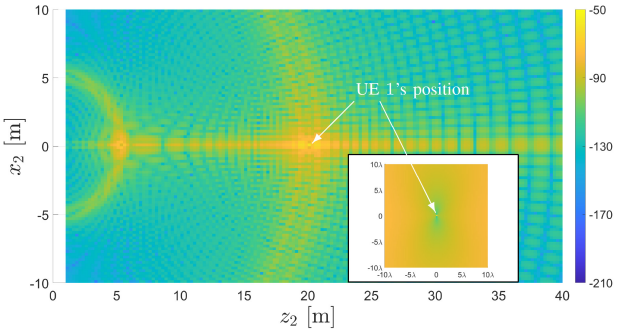

(a) MMSE combining.

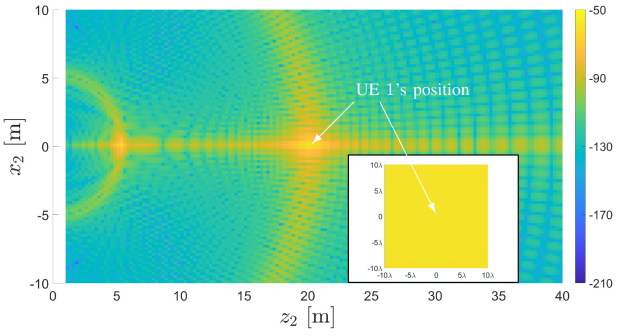

(b) MR combining.

Fig. 5. Interference gain behavior using the *mismatched* model for a fixed UE as a function of different locations of an interfering UE.

(at the same height as UE 1). We assume $f_0 = 28\,\text{GHz}$ and consider both MR and MMSE. Note that, at $f_0 = 28\,\text{GHz}$, $d_F \approxeq 233.3\,\text{m}$, and hence both UEs are in the NF region.

Fig. 4 reports the normalized gain with the exact model. MMSE and MR combining are used in Figs. 4(a) and 4(b), respectively. Each figure contains a magnification around UE 1's location, in which the relative distance of UE 2 from UE 1 is measured in λ (for a total span of around $0.11 \times 0.11\,\text{m}^2$). Fig. 4(a) shows that the interference with MMSE is high only in a small region around UE 1, whose semi-major axis (along both directions) is fractions of λ. This means that MMSE can efficiently reject any interference that comes from a location that is at least a few centimeters away. On the contrary, Fig. 4(b) shows that MR experiences high interference from locations that are either along the Z direction or along a semi-circle with radius equal to the distance of UE 1.

Fig. 5 plots the results obtained with the mismatched model. Unlike Fig. 4, we now see that the interference gain with the two combining strategies exhibits a similar behaviour. The impact of the mismatched model is particularly evident with the MMSE combiner. In particular, we observe that the lower values of the interference gain are at least three orders of magnitude higher than those in Fig. 4 (note that the same colorbar scale is used in all figures, including the magnifications). The conclusion is that MMSE can suppress interference much more efficiently when used with the exact model, whereas MR is greatly suboptimal in both cases.

C. Spectral Efficiency Analysis

We now evaluate the SE of a single-cell network, assuming that K UEs are randomly displaced in the sector $[-\pi/3, +\pi/3)$ with a minimum distance of 15 m from BS.

Fig. 6 reports the cumulative distribution function (CDF) of the SE achieved by MMSE and MR when the carrier frequency is $f_0 = 5\,\text{GHz}$, $28\,\text{GHz}$, and $71\,\text{GHz}$. The number of UEs is $K = 100$, and the cell radius is $R = 230\,\text{m}$, which corresponds approximately to the Fraunhofer distance at $28\,\text{GHz}$, and is in line with current 5G cell sizes. The dashed and solid refer to the results obtained with the exact and mismatched model, respectively. Let us focus on the results of Fig. 6(a), obtained with the MMSE combiner. For all frequencies, the performance using the exact model to build the combiner is much better than the one obtained with the mismatched model. However, increasing the carrier frequency has a two-fold beneficial impact on the SE. On the one hand, the average SE increases as f_0 increases. On the other hand, the CDF with the exact model exhibits a steeper behavior, meaning that more fairness across the UE positions is guaranteed. The conclusion is that the use of the exact model dramatically improves the interference suppression capabilities of MMSE combining. This is not the case with MR combining. Indeed, Fig. 6(b) shows that only marginal differences exist between exact and mismatched models, including the fairness properties.

A similar conclusion can be drawn in Fig. 7(a), which collects the CDFs for the SE achieved by MMSE and MR combiners for a variable number of UEs ($K = 50$, 100, and 150) when $f_0 = 28\,\text{GHz}$ and $R = 230\,\text{m}$. The results are only marginally affected by the number of UEs when the exact model is used (dashed lines). This is not true for the combiners based on the mismatched model (solid lines) and/or based on MR combining (not reported here for the sake of brevity, as, similarly to Fig. 6(b), both models provide very similar results when using MR combining). The same conclusion applies on the fairness performance, which is guaranteed

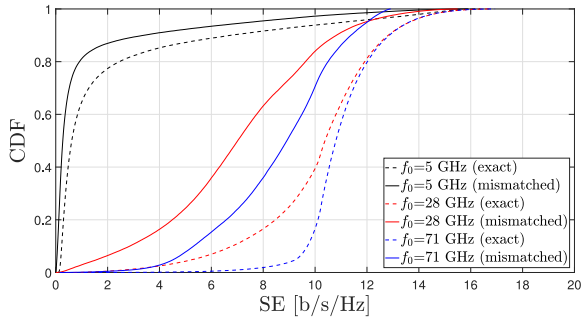

(a) MMSE combining.

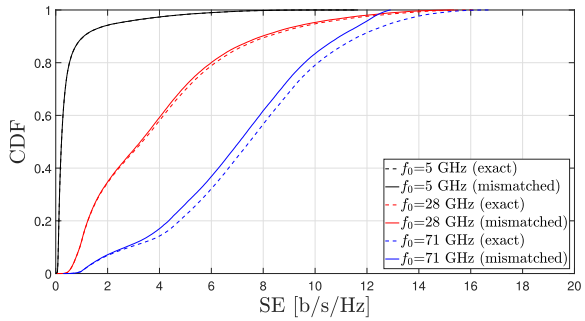

(b) MR combining.

Fig. 6. CDF of the SE as a function of the carrier frequency when $K = 100$ and $R = 230\,\text{m}$, corresponding to the Fraunhofer distance at 28 GHz.

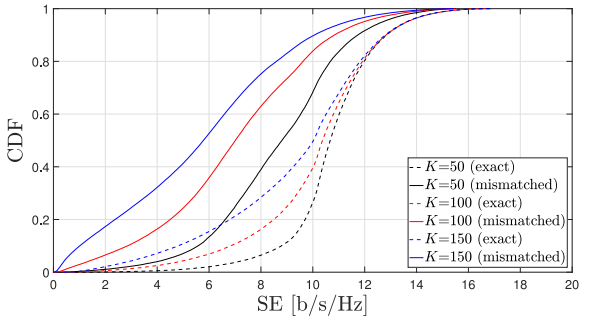

(a) CDF of the SE with MMSE combining for different values of K.

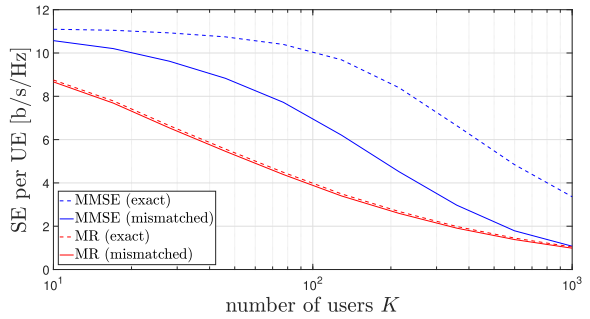

(b) SE per UE of both MMSE and MR as a function of K.

Fig. 7. Impact of the number of active UEs on the SE performance.

by the usage of MMSE combining based on the exact model.

To further quantify the benefits brought by MMSE combining with the exact model, Fig. 7(b) provides the average SE per UE as a function of K. The cell sector radius R is 230 m, and the carrier frequency is $f_0 = 28\,\text{GHz}$. As can be seen, the gap between the exact and mismatched models is very significant. Moreover, the SE maintains nearly flat as K increases up to $K = 100$, which translates into a density of around 1500 devices/km^2 per channel use, as requested in 5G [9]. Note that the excellent interference suppression capabilities let MMSE based on the exact model maintain the gap with other schemes when K reaches very large values. The same trend is confirmed when measuring the average SE per UE as a function of R (not reported for the sake of brevity): the performance gap using current 5G frequencies is very significant for $R \leq 50\,\text{m}$, and even more significant when considering sub-THz frequencies and smaller cell sizes.

IV. Conclusion

The main conclusion of this letter is that it is time for multi-user MIMO communication theorists to abandon the FF approximation when considering carrier frequencies above 6 GHz. We instead need to consider more complicated channel models that capture the radiative NF characteristics, in particular concerning the spherical phase variations. This also affects beamforming codebooks. We showed that interference-aware combining schemes based on the radiative NF model can effectively exploit the extra degrees-of-freedom offered by the propagation channel to deal with interference so as to enhance the scalability (in terms of number of UEs) and fairness of the system. This applies already to 5G multi-user MIMO communications above 6 GHz (e.g., in the range of mm-Wave bands), and will be further exacerbated by beyond-5G communications, operating in the sub-THz spectrum.

References

[1] T. S. Rappaport et al., "Wireless communications and applications above 100 GHz: Opportunities and challenges for 6G and beyond," *IEEE Access*, vol. 7, pp. 78729–78757, 2019.

[2] *Technical Specification Group Radio Access Network; NR; Physical Channels and Modulation (Release 17), V17.3.0*, 3GPP Standard TS 38.211, Sep. 2022.

[3] R. W. Heath and A. Lozano, *Foundations of MIMO Communication*. Cambridge, U.K.: Cambridge Univ. Press, 2018.

[4] K. T. Selvan and R. Janaswamy, "Fraunhofer and fresnel distances: Unified derivation for aperture antennas," *IEEE Trans. Antennas Propag.*, vol. 59, no. 4, pp. 12–15, Aug. 2017.

[5] H. Do, S. Cho, J. Park, H.-J. Song, N. Lee, and A. Lozano, "Terahertz line-of-sight MIMO communication: Theory and practical challenges," *IEEE Commun. Mag.*, vol. 59, no. 3, pp. 104–109, Mar. 2021.

[6] F. Bøhagen, P. Orten, and G. E. Øien, "On spherical vs. plane wave modeling of line-of-sight MIMO channels," *IEEE Trans. Commun.*, vol. 57, no. 3, pp. 841–849, Mar. 2009.

[7] E. Torkildson, U. Madhow, and M. Rodwell, "Indoor millimeter wave MIMO: Feasibility and performance," *IEEE Trans. Wireless Commun.*, vol. 10, no. 12, pp. 4150–4160, Dec. 2011.

[8] B. Friedlander, "Localization of signals in the near-field of an antenna array," *IEEE Trans. Signal Process.*, vol. 67, no. 15, pp. 3885–3893, Aug. 2019.

[9] "Minimum requirements related to technical performance for IMT-2020 radio interface(s)," ITU, Geneva, Switzerland, Rep. ITU-R M.2410-0, Nov. 2017.

[10] E. Björnson and L. Sanguinetti, "Power scaling laws and near-field behaviors of massive MIMO and intelligent reflecting surfaces," *IEEE Open J. Commun. Soc.*, vol. 1, pp. 1306–1324, 2020.

[11] D. Dardari, "Communicating with large intelligent surfaces: Fundamental limits and models," *IEEE J. Sel. Areas Commun.*, vol. 38, no. 11, pp. 2526–2537, Nov. 2020.

[12] E. Björnson, Ö. T. Demir, and L. Sanguinetti, "A primer on near-field beamforming for arrays and reconfigurable intelligent surfaces," in *Proc. Asilomar*, Pacific Grove, CA, USA, Nov. 2021, pp. 105–112.

[13] E. Björnson, J. Hoydis, and L. Sanguinetti, "Massive MIMO networks: Spectral, energy, and hardware efficiency," *Found. Trends Signal Process.*, vol. 11, nos. 3–4, pp. 154–655, 2017.

[14] Ericsson. "Massive MIMO Solutions Accelerate 5G Mid-Band." 2022. [Online]. Available: https://www.ericsson.com/en/ran/massive-mimo

[15] H. Lu and Y. Zeng, "Near-field modeling and performance analysis for multi-user extremely large-scale MIMO communication," *IEEE Commun. Lett.*, vol. 26, no. 2, pp. 277–281, Feb. 2022.

Open Access funding provided by 'Università di Pisa' within the CRUI CARE Agreement